Electric Field-driven Fused Deposition of High-resolution Polycaprolactone Microstructures

Fulai Cao, Yanpu Chao*, Shuai Lu, Ruirui Guo and Yaohui Li

Abstract—**Polycaprolactone (PCL) fibers have been widely used in the preparation of biological scaffolds. However, near-field electrospinning and melt electrospinning limitations in terms of molding height and residual charge, make it difficult to fabricate high-resolution complex PCL microstructures. This study proposes an electric field-driven melting deposition technique for direct writing of high-resolution PCL microstructures, which can be used to fabricate PCL micro-scaffolds. The basic process principle of continuous cone jet mode was analyzed, an electric field-driven melting deposition-based direct writing system was developed, and single-layer and multi-layer deposition experiments were systematically conducted. Further, the effect of collecting plate velocity on deposition morphology was investigated. The single-layer raster and grid structures were prepared. A model was established to predict the forming height of a single deposition line based on the deposition line width and solidification angle. The multi-layer deposition and direct writing of the "wall" structure was observed, and the multi-layer "wall" structure and the ring structure with a high aspect ratio were prepared.**

Index Terms—**Electric field-driven, Polycaprolactone, Microstructure, Taylor cone, Large aspect ratio**

I. INTRODUCTION

MICRO/NANO three-dimensional (3D) printing, a novel form of micro/nano processing technology, has emerged in recent years and is steadily becoming a key technology in the field of precision machining [1, 2]. Traditional micro/nano machining methods such, as micromachining, micro hot pressing, and laser etching, have shown significant shortcomings in processing accuracy and quality. Such technologies are usually applied for fabricating 2D micro/nano structures and are unable to fabricate complex and multi-material 3D micro/nano structures. In contrast, micro/nano 3D printing offers outstanding advantages in fabricating complex 3D structures, those with large aspect ratios, composite formulations, etc. [3]. It has been extensively used in biomedical, micro-electro–mechanical systems, micro/nano optics, micro-actuators [4, 5], and many other fields.

Current representative micro/nano 3D printing processes mainly include projected microstereolithography (PµSL), two-photon polymerization (TPP), focused ion beam direct writing (FIBDW), focused electron beam (FEB)-induced deposition, micro laser sintering technology (MLS), electrochemical fabrication (EFAB), and electrohydrodynamic (EHD) jet printing. TPP and PµSL utilize photocuring of laser-induced photosensitive materials [6], although the choice of materials is limited. Furthermore, FIBDW and FEB-induced deposition equipment are expensive and involve high manufacturing costs [7]. MLS and EFAB are mainly used for micro/nano 3D printing of metallic materials [8]. However, EHD jet printing has received a lot of attention in recent years due to its advantages, such as simple structure, cost-effectiveness, no requirement for masks or molds, and the possibility of multi-material printing [9]. Thus, the exploration and development of near-field electrospinning (NFES) technology and the application of fibers have become the research hotspot.

NFES technology has led to rapid development in the research and preparation of micro/nano structures of organic polymers and their functional devices. Among them, highly oriented or regularly arranged micro/nano structures show good performance in the field of tissue engineering due to their anisotropy [10]. For instance, Mai et al. [11] prepared 20 layers of polycaprolactone (PCL)/collagen composite fibers by NFES technology, and the microfibers exhibited good antimicrobial, hydrophilic, and water-absorbent properties. Kolan et al. [12] discussed the cell viability of PCL/bioactive glass (13-93B3) composite scaffolds prepared by NFES technology and demonstrated that the biomimetic scaffolds prepared by NFES technology had a high cell proliferation rate. Garcia-Galan et al. [13] mixed a photocurable resin with ceramic paste and obtained a multi-layer bioceramics grid scaffold with a diameter of 80 µm through NFES and photocuring technology. Wang et al. [14] prepared PCL/hydrogel composite scaffolds loaded with mesenchymal stem cells by NFES technology, which showed a significant

Fulai Cao is a lecturer of School of Electrical and Mechanical Engineering, Xuchang University, Xuchang 4561000, China. (e-mail: cfulai@163.com).

Yanpu Chao is a professor of School of Electrical and Mechanical Engineering, Xuchang University, Xuchang 4561000, China. (Corresponding author to provide e-mail: chaoyanpu@163.com).

Shuai Lu is a lecturer of School of Electrical and Mechanical Engineering, Xuchang University, Xuchang 4561000, China. (e-mail: zdlu996@126.com).

Ruirui Guo is a lecturer of School of Electrical and Mechanical Engineering, Xuchang University, Xuchang 4561000, China. (e-mail: guoruirui2527@163.com).

Yaohui Li is an associate professor of School of Electrical and Mechanical Engineering, Xuchang University, Xuchang 4561000, China. (e-mail: liyaohui1008@163.com).

improvement in the mechanical properties over traditional hydrogel scaffolds.

However, most of the biomaterials required for the NFES technique need to be dissolved in toxic organic solvents such as chloroform, methanol, and *N,N*-dimethylformamide for electrostatic spinning, therefore, the orientation pattern of the prepared fibers can adversely affect the cell culture.

In melt electrospinning writing (MEW), the biopolymer material is heated to a molten state before precise fiber deposition. This technique avoids the use of toxic organic solvents and can increase the biocompatibility of fiber patterns. Compared with the polymer solution, the polymer melt can be rapidly cooled during the spraying process, and the fibers are vertically lapped together. It increases the scaffold void connectivity [15], facilitates metabolic waste discharge and nutrient supply, and increases cell survival, making it a promising candidate for tissue engineering.

PCL scaffold is composed of micro/nano fibers that are biocompatible, degradable, non-toxic, and designable. PCL scaffold prepared by melt electrospinning direct writing technology offers a wide range of application prospects in tissue engineering. For instance, Hochleitner et al. [16] explored the lower limit of the resolution of MEW and prepared 3D poly-epsilon-caprolactone coherent scaffolds with a minimum linewidth of 817±165 nm, a period of 100.6±5.1 μm, and a height of 80 μm. Großhaus et al. [17] improved the nozzle structure based on predecessors and reduced the average minimum diameter of the fiber to 275±86 nm. Chen et al. [18, 19] examine how MEW technical parameters (spinning voltage, collector plate moving speed, receiving distance, and melt temperature) and material mixing ratio affect the properties of PCL/nano-hydroxyapatite composite scaffolds. Shi et al. [20] reported a method to improve the cell affinity and osteogenic induction properties of melt electrospinning-written PCL scaffolds.

Although NFES and MEW facilitate the printing and precise deposition of micro/nano fibers, as well as the preparation of biological scaffolds with the characteristic size of cells, they require the use of a grounded electrode in the printing process [21], which requires the printing voltage to become continuously larger with the increase in the height of the print, and it is often difficult for the print height to exceed 5 mm. Therefore, larger-size objects and macro/micro composite structures cannot be manufactured on existing macro entities. Moreover, due to the influence of residual charge, when the printing cycle is relatively small, a rejection reaction occurs between adjacent fibers [22], which reduces the deposition accuracy and leads to uneven porosity.

To address the issue of printing biological scaffolds by electrostatic spinning technology, an electric field-driven melting deposition-based direct writing of high-resolution PCL microstructure is proposed, which can be used to fabricate high-performance multilayer biological scaffolds. Furthermore, the process principle of this technology is analyzed, the single-layer and multi-layer deposition experiments are conducted, and the influence of the movement speed of the collecting plate on the morphology of the fiber deposition is investigated. Finally, the raster structure, grid structure, high aspect ratio "wall", and ring structure are prepared.

II. PROCESS PRINCIPLE

Electric field-driven melt deposition-based direct writing is a digital manufacturing process that can directly write high-resolution patterns on the collecting plate. To stimulate the electric field required for injection through electrostatic induction, it is necessary to connect the conductive nozzle to the positive electrode of the high-voltage pulse power supply without grounding the negative electrode. The basic working principle is shown in Fig. 1. In the absence of an applied electric field, as shown in Fig. 1(a), the molten print material inside the nozzle slides downward to flow out of the nozzle under gravity and air pressure. Under the combined effect of air pressure, gravity, viscous forces, and surface tension, the material coming out of the nozzle is in the form of a curved moon face and remains stable. At the beginning of direct writing, the nozzle is connected to the positive electrode of the direct current (DC) high-voltage power supply. When the nozzle is near the substrate, the positive and negative charges in the substrate get rearranged due to the electrostatic

(a) The state when no electric field is applied

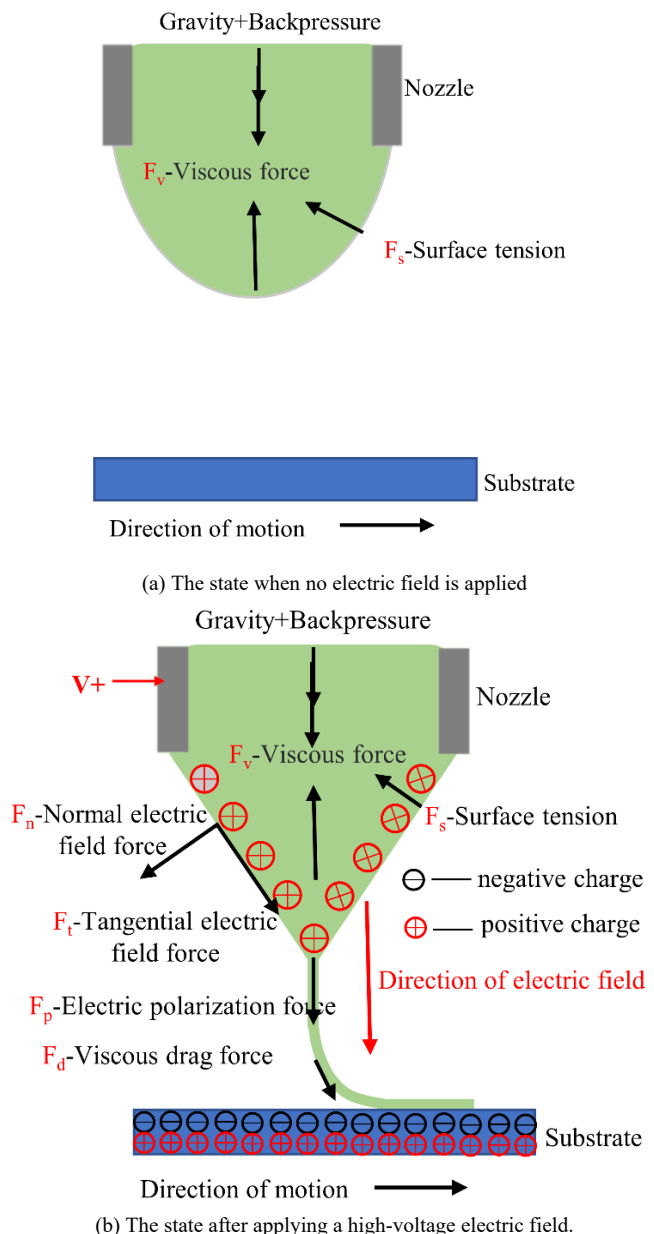(b) The state after applying a high-voltage electric field.
Fig. 1. The principle of electric field-driven fused deposition process

induction, as shown in Fig. 1(b). The negative charges are attracted and they gather on the upper surface of the substrate, while the positive charges are repelled and gathered on the lower surface of the substrate. The electric field required for spraying is generated between the nozzle and the substrate. The droplet at the nozzle position is polarized by the electric field, and the positive charge continuously accumulates on its surface. Under the combined action of the electric field force (Ft-tangential electric field force, Fn-normal electric field force, Fp-polarized electric field force), surface tension (Fs), viscous force (Fv), gravity (Fg), and backpressure (Fb), the droplet gradually elongates until the Taylor cone shape is formed.

When the voltage is continuously increased, once the electric field force exceeds the liquid surface tension and viscous force, the tip of the Taylor cone sprays out a very fine jet (jet diameter is usually 1–2 orders of magnitude smaller than the nozzle size). After the jet contacts the collection plate, the fiber diameter is further reduced under the action of the viscous drag force (Fd), and the direct writing of the microfiber is realized. When the first layer is printed on the collector plate, the Z-axis stage is raised by one printing layer thickness, and the electric field continues to undergo excitation between the conductive nozzle and the printed entity to print the next layer of the structure. This process thus avoids the problem encountered during electrostatic spinning technology that needs to increase the voltage with the increase in the height of the printed prototype. High-resolution 3D solid writing can be achieved by repeating the above-mentioned process.

III. Experimental System and Materials

A. Experimental system

The experimental system for the electric field-driven fused deposition direct writing mainly includes DC high-voltage power supply, real-time observation device, control computer system, nozzle, nozzle heating block, quartz crucible, temperature controller, annular heating furnace, pneumatic pressure control unit, collection plate, and multi-axis motion platform, as shown in Fig. 2. To ensure the complete melting of the PCL material, the temperature controller was used to regulate the temperature of the annular heating furnace to maintain the crucible at a constant temperature of 125 °C. The pressure control unit (including an air pump and a precision pressure regulator) was used to control the liquid flow, in order to stabilize the molten PCL at the bottom of the nozzle in a meniscus shape. Moreover, the nozzle temperature was maintained at 85 °C under the action of the nozzle heating block and the temperature controller, which provided stable conditions for the injection process. The multi-axis movement platform consists of a high-precision X–Y axis movement platform and a Z-axis movement platform, in which the collection plate is fixed on the X–Y movement platform to complete the planar 2D movement, and the nozzle is fixed on the Z-axis movement platform to complete the relative height movement with the collection plate. The three-dimensional movement of the nozzle is accomplished by combining movements along three axes. The positive electrode of the DC high-voltage power supply is connected to the nozzle to provide the system with the high
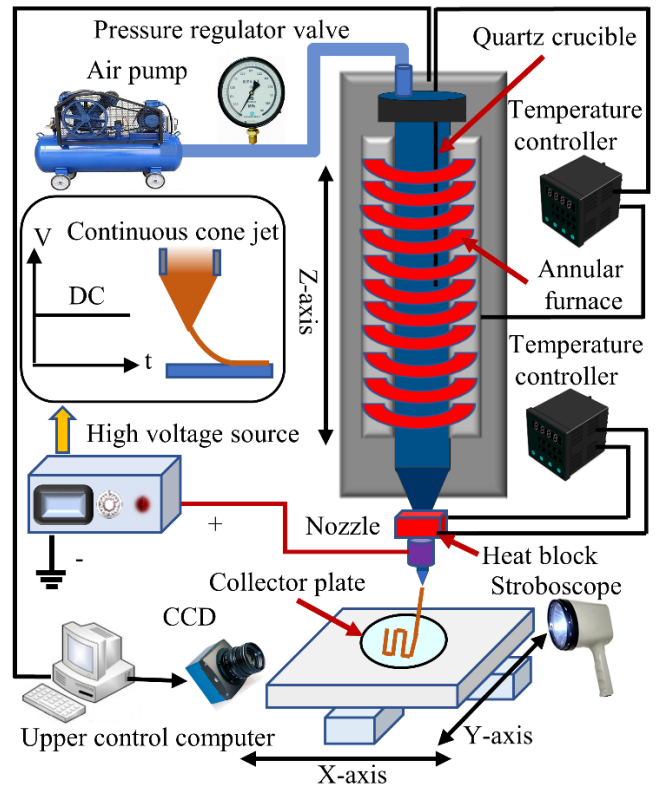

Fig. 2. Schematic of experimental system for electric field-driven molten deposition-based direct writing.

voltage required for injection. The upper control computer system is capable of controlling the precise motion of the multi-axis motion platform as well as real-time observation and recording of the CCD camera. During the experiment, molten PCL was ejected from the nozzle to form a jet under the action of a high-voltage electrostatic field, and its motion and deposition process were observed and recorded using a CCD camera. Printing was carried out layer by layer according to the printing path generated by the 3D model, and finally, the high-resolution manufacturing of PCL microstructures was realized.

B. Experimental materials

Granular PCL produced by Shandong Yusuo Chemical Technology Co., Ltd. was selected for the experiment, and its performance parameters are listed in Table I.

TABLE I
PCL Performance Parameters

Properties	Test data
Molecular formula	$(C_6H_{10}O_2)_n$
CAS NO	24980-41-4
Molecular weight	37,000–80,000
Melting point/°C	60
Viscosity of liquid after melting/(dL·(Gm)$^{-1}$)	11.25
Density/(g·mL^{-1})	1.145 (26 °C)

TABLE II
Experimental Parameters of Linear Deposition

Parameters	Values
Printing Substrate	Polyethylene terephthalate (PET)
Deposition Height/H (μm)	300
Pulse voltage/U (V)	1,700
Nozzle diameter/D (μm)	300
Crucible temperature/Tc (°C)	125
Air pressure/(KPa)	15
Nozzle temperature/Tn (°C)	85
Moving speed/V (Plus·s^{-1})	F0, F50, F100, F350

IV. EXPERIMENTAL STUDY ON DIRECT WRITING OF MONOLAYER DEPOSITION

A. Influence of the collecting plate velocity on the morphology of fiber deposition

The orderly deposition and controlled formation of jet fibers are the main objectives of electric field-driven melting deposition-based direct writing. Moreover, these factors are also the basis for the preparation of multilayer complex microstructures. In addition to the electric field force, gravity, and surface tension, the jet of this direct writing process is also subject to the traction force of the collecting plate. Moreover, the moving speed of the collecting plate is an important factor affecting the collection performance of the jet fiber orientation, thus it is necessary to systematically investigate the effect of the moving speed of the collecting plate on the deposition.

The results reveal that the deposition pattern changes with the velocity of the collecting plate, which is related to the relationship between the velocity V_f when the liquid line falls to the collecting plate and the velocity V_s of the collecting plate itself. When $V_s < V_f$, the jet hits the collection plate and deforms due to the force. Owing to the small diameter of the fibers, they are easily affected by electric field force and other factors, resulting in the whipping effect. This causes the bottom of the liquid line to rotate or swing near the collector plate in the vertical direction, leading to a curled pattern or Z-shape pattern in the deposited material, as shown in Figs. 3(a) and 3(b). For $V_s \approx V_f$, when the jet is deposited on the collection plate, it is pulled along the movement direction of

the collection plate, but due to the small traction force, it cannot pull the whipped fibers to form a catenation state. At this time, the deposition pattern changes from bending to a critical state of straight lines, as shown in Fig. 3(c). This process favors the straightening of the whipped fibers, which is called "unwinding". When $V_s > V_f$, the jet deposition on the collection plate is subjected to a pulling force along the movement direction of the collection plate, and the jet is pulled to form a catenated state, resulting in a straight line deposition pattern, as shown in Fig. 3(d). In this process, the relative movement of the nozzle and collector plate continuously stretches the jet or fiber, resulting in its thinning, which is commonly referred to as "shaping".

Under the experimental conditions listed in Table II, the motion velocity of the deposition collecting plate was adjusted to F0, F40, F100, and F350, and the corresponding deposition patterns were observed. When the motion velocity of the deposition collecting plate was F0, the jet impinged on the collection plate and produced spiral fluctuations in the vertical direction, resulting in an irregular curling pattern with low deposition accuracy, as shown in Fig. 3(e). When the moving speed of the collecting plate was F50, the collecting plate exerted a stretching effect on the jet, reducing the spiral fluctuation of the jet deposition and resulting in a relatively regular Z-shape pattern, as shown in Fig. 3(f). When the motion speed of the deposition collecting plate was increased to F100, the spiral fluctuation disappeared, and the curvature of the deposition line gradually decreased and shifted to a straight shape, as shown in Fig. 3(g). When the

(a) $V_s < V_f$ (curled pattern) (b) $V_s < V_f$ (Z-shape pattern) (c) $V_s \approx V_f$ (d) $V_s > V_f$

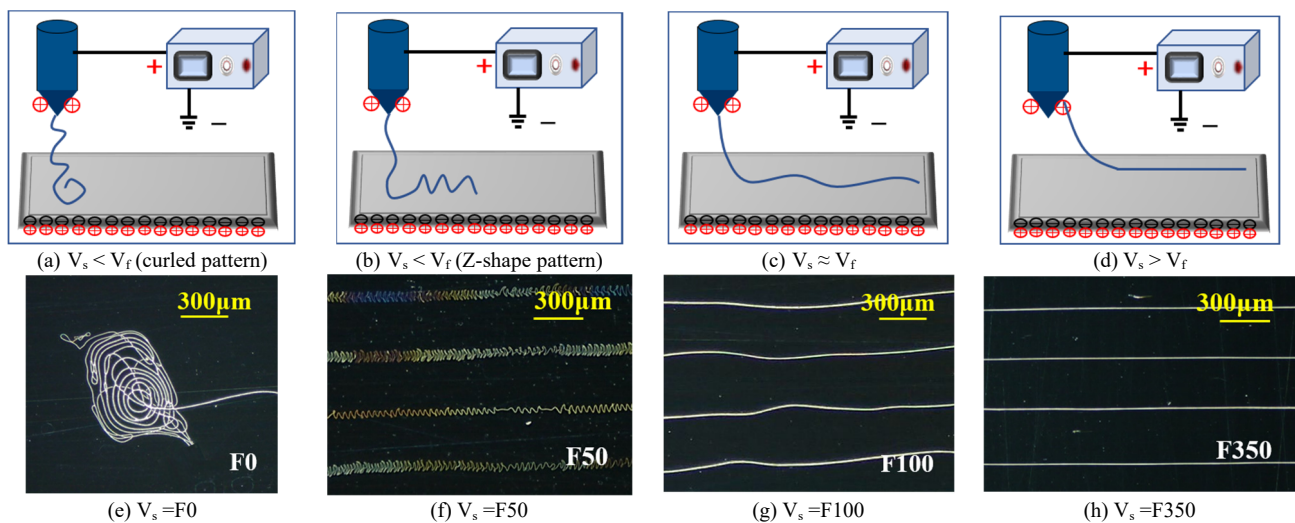(e) $V_s =$F0 (f) $V_s =$F50 (g) $V_s =$F100 (h) $V_s =$F350

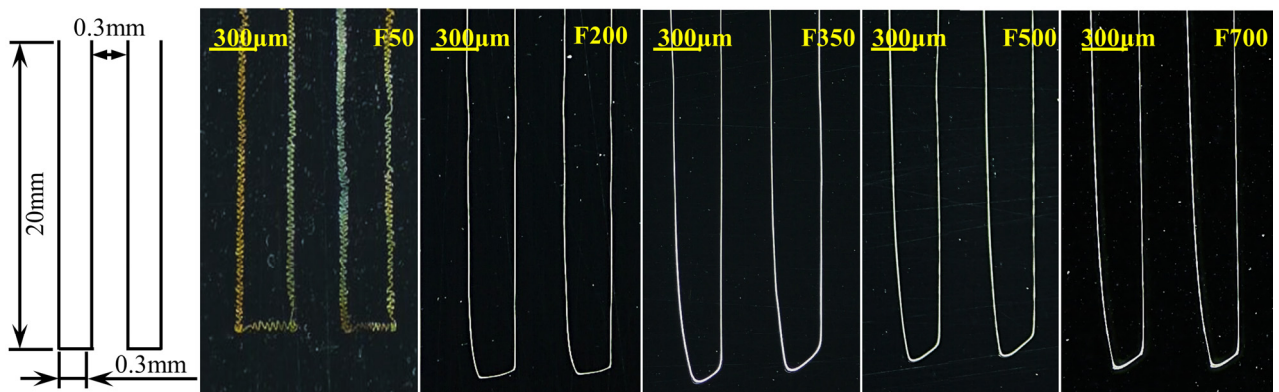Fig. 3. Morphology of deposition lines at different speeds of the collecting plate.

Fig. 4 Morphology of the right Angle of the parallel line at different speeds of the collecting plate.
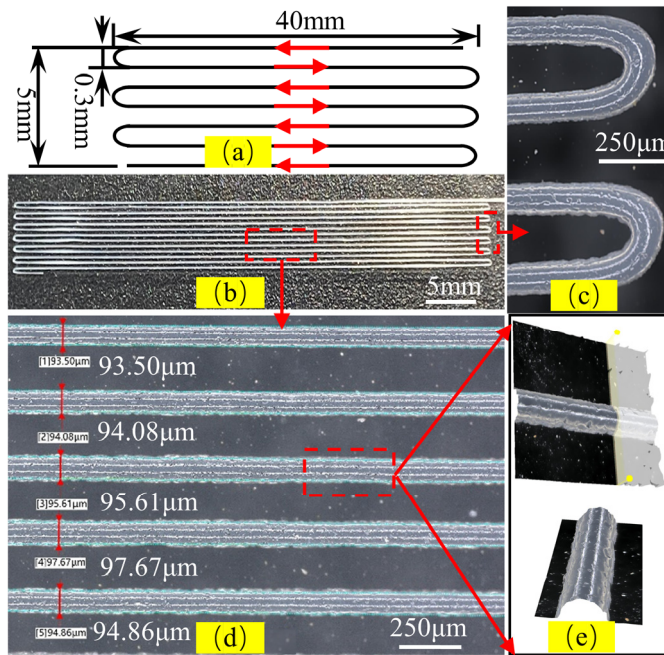
Fig. 5 Structural morphology of single-layer raster: (a) Raster printing path, (b) Macroscopic image of the raster, (c) Microstructure at the raster parallel lines, (d) Microstructure at the corner of the raster arc, and (e) 3D structure of a single line.

TABLE III
EXPERIMENTAL PARAMETERS OF RASTER STRUCTURE

Parameters	Values
Printing Substrate	Glass slide
Deposition Height/H (μm)	200
Pulse voltage/U (V)	1,800
Nozzle diameter/D (μm)	300
Crucible temperature/Tc (°C)	125
Air pressure/(KPa)	15
Nozzle temperature/Tn (°C)	85
Moving speed/V (Plus·s^{-1})	F40
Grating period/(μm)	300

TABLE IV
EXPERIMENTAL PARAMETERS OF GRID STRUCTURE

Parameters	Values
Printing Substrate	PET
Deposition Height/H (μm)	300
Pulse voltage/U (V)	1,700
Nozzle diameter/D (μm)	300
Crucible temperature/Tc (°C)	125
Air pressure/(KPa)	15
Nozzle temperature/Tn (°C)	85
Moving speed/V (Plus·s^{-1})	F350
Grating period/(μm)	300

motion speed of the deposition collecting plate was increased to F350, the tensile force of the collection plate played a leading role, and the jet was stretched and deposited in a straight-line shape. Moreover, the spacing between lines was very uniform and the direct writing state was very stable, as shown in Fig. 3(h).

B. Influence of collecting plate speed on corner fiber deposition

Owing to the viscoelastic properties of molten materials, a lag is observed in melt deposition, and the deposited fibers can never reach the end of the parallel path, which affects the deposition at the corner of the matrix. Fig. 4 shows the fiber deposition morphology at the corner of the parallel lines of the matrix. When the movement speed of the collecting plate is low at F50, although the corners have an angle of 90°, the deposited fibers fluctuate significantly and appear in a Z-shape, resulting in poor deposition accuracy. When the velocity is F200, the fluctuation of the deposited fibers is reduced, the corner pattern is more complete, and the deposition accuracy is increased, but the linearity of the deposited line needs to be improved. When the movement speed of the collecting plate continues to increase to F350, F500, and F700, although the linearity of the deposition line is good, the trajectory of the corner cannot be accurately written directly. Moreover, the faster the movement of the collecting plate, the greater the deformation of the corner pattern, and the liquid accumulation phenomenon occurs at the corner. Therefore, when the matrix parallel lines are written directly, the linearity of the deposition line and the integrity of the corner right angle cannot be achieved at the same time. To reduce the influence of hysteresis on the arrangement of the fibers to be deposited, the corner right angle can be changed to an arc.

C. Direct writing of single-layer raster structure

Fig. 5 shows a single-layer raster structure written directly on a slide using the process parameters listed in Table III. The raster printing path is shown in Fig. 5(a), which has a 0.3 mm diameter arc at the corners, an area of 40 mm × 5 mm, and a period of 300 μm. Fig. 5(b) exhibits the macroscopic image of the raster, indicating the absence of defects in the structure, and the deposition lines are relatively uniform. Fig. 5(c) shows the microstructure at the raster parallel lines. The measured single line widths are 93.50, 94.08, 95.61, 97.67, and 94.86 μm, and the average line width of the deposition lines is 95.15 μm. Fig. 5(d) shows the microstructure at the corner of the raster arc, exhibiting that the deposition position of the liquid line is the same as the set arc path, and there is no material accumulation at the end of the path. Fig. 5(e) shows the 3D structure of a single line. In general, the structural features and structure size (line width, period) are consistent with the expected design of the graphic structure geometry.

Fig. 6 shows the longitudinal section profile of the raster in the same plane. The four sections have similar shapes and are approximately bow-shaped, with their chord length equal to the line width of the raster and an acute solidification angle between the deposition line and the slide. Fig. 7 shows the vertex cross-section contour of a single deposition line, revealing that the vertex contour fluctuates slightly. The maximum measured height of the vertex is 39.07 μm, with a minimum of 36.45 μm and an average of 37.56 μm. The aspect ratio of a single deposition line is 0.39:1.

Fig. 8 shows the shape parameters of a longitudinal section of the deposition line. The ideal longitudinal section outline is a regular circular arc, and the deposition height can be expressed as follows:

When $0° < \theta \leqslant 90°$

$$H = R - R\cos\theta$$
$$\sin\theta = L/2R \tag{1}$$

$$H = \frac{L}{2\sin\theta} - \frac{L}{2}\cot\theta$$

When $90° < \theta < 180°$

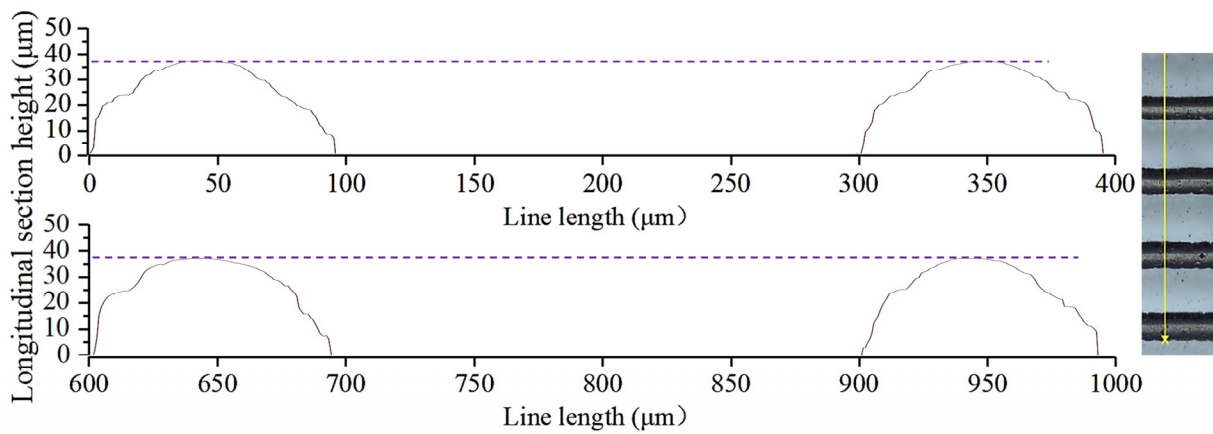$$H = R + R\sin(\theta - \pi/2)$$
$$L = 2R \tag{2}$$
$$H = L(1 - \cos\theta)/2$$

Fig. 6 Outline of the longitudinal section of the raster
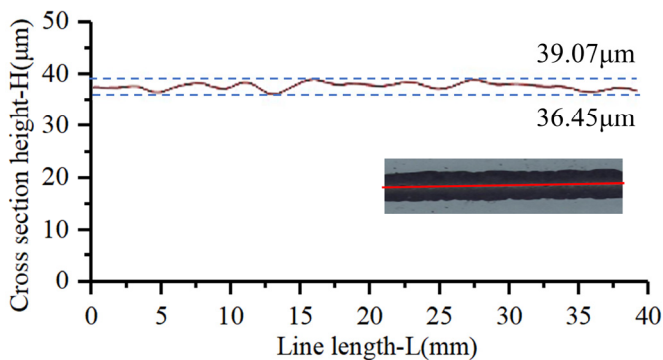
Fig. 7 Vertex cross-section profile of a single deposition line

Fig. 8 Shape parameter model of the longitudinal section of sedimentary line

where L is the maximum forming width, H is the forming height, and θ is the solidification angle. After measurement, the solidification angles of the left and right sides of molten PCL on the slide are 73.4° and 72.8° respectively. The average value of 73.1° is considered as the solidification angle of PCL on the slide, the maximum forming line width $L = 95.15$ μm is put into Equation (3), and $H = 35.27$ μm is obtained. Compared with the actual measurement value of 37.86 μm, the error is 6.8%, thus the model can effectively predict the forming height of a single deposition line by using the deposition line width and solidification angle.

D. Direct writing of single-layer grid structure

Grid structures are the most common scaffold structures in tissue engineering. The patterned grid structures can be prepared by the electric field-driven fused deposition direct writing technique, and the size of the grid can be precisely controlled. Fig. 9 shows the crossed lattice structures, prepared under the experimental conditions listed in Table IV, and their motion trajectories are shown in Fig. 9(a). Fig. 9(b) exhibits the macro image of the cross grid, with a size of 12 mm × 8 mm and a period of 300 μm. Fig. 9(c) shows a magnified grid image, revealing good linearity and uniform diameter of the deposited fibers. The grid deposited line width measured using Image Pro software is 9.43 μm. To ensure the measurement accuracy when measuring the side length of the grid, the grid was taken as half of the diameter of each side fiber. The measured size of the grid was 300±6.56 μm, which is consistent with the designed side length of 300 μm. Moreover, the error was about 2.19%, indicating that the fiber deposition trajectory can closely follow the trajectory of the moving platform and that the two trajectories are consistent.
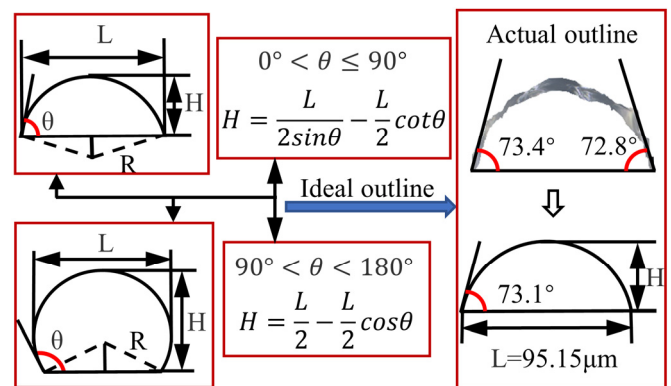
V. EXPERIMENTAL STUDY ON DIRECT WRITING OF MULTILAYER DEPOSITION

A. Direct writing of multilayer "wall" structures

Large aspect ratio microstructures are widely used in the fields of micro batteries, transparent electrodes, 3D integrated circuits, sensors, etc [23]. However, it is difficult to achieve cost-effective and simple fabrication of microstructures with large aspect ratios by traditional processing technology. Electric field-driven melt deposition direct writing technology provides a new method for fabricating high-aspect-ratio microstructures, with low manufacturing costs and a short production cycle. Fig. 10 shows the process of direct writing via multi-layer deposition. The experimental parameters are the same as those for the raster structure, and the nozzle rises by 0.1 mm for each layer deposited. Because of the existence of direct writing height, the jet deposited on the slide is pulled along the direction of movement, and the jet is "pulled" to form a catenary state. At this time, there is a certain dragging distance, and the angle between the jet and the vertical direction is the deflection angle α.

Fig. 10(a) shows the stable state of deposition of the first layer. In this case, droplets at the nozzle gather on the left side of the nozzle center due to the pulling force of the collection plate, resulting in a liquid line deflection angle α of 41.02°. Fig. 10(b) shows the stable state of deposition of the second layer. The collecting plate moves in the opposite direction, causing droplets to gather on the right side of the nozzle center. This results in a liquid line deflection angle of 47.58°.
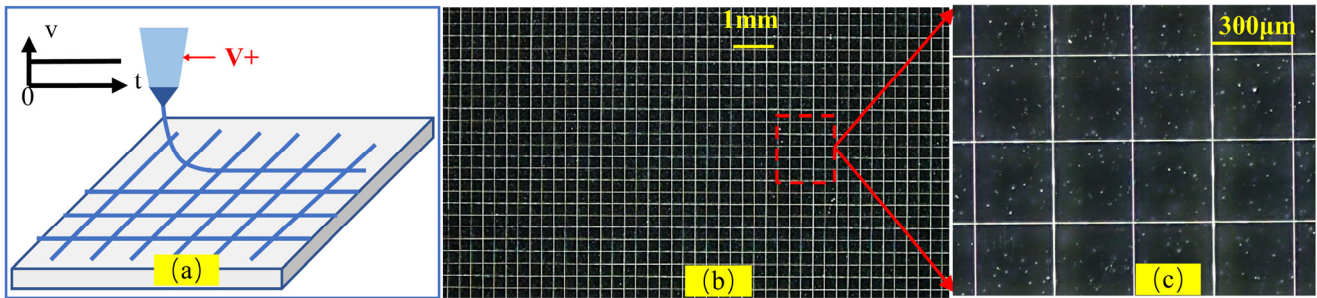
Fig. 9: Mesh structure morphology. (a) Written motion trajectories. (b) Macro image of the cross grid. (c) Enlarged view of the grid.
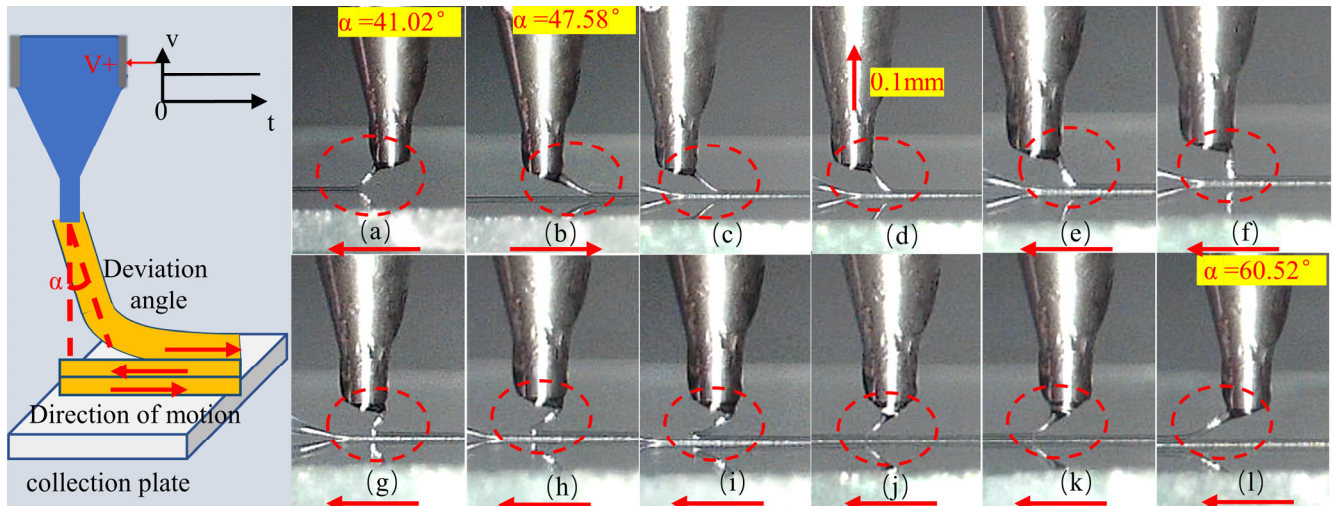

Fig. 10 Process of multi-layer deposition direct writing. (a) Stable state of deposition of the first layer. (b) Stable state of deposition of the second layer. (c) ~ (l) Deposition process of the third layer.

Figs. 10(c)–10(l) show the deposition process of the third layer. When the collecting plate moves in the right direction to the end of the deposition path of the second layer, as shown in Fig. 10(c), the second layer deposition ends, and the nozzle is raised by 0.1 mm, as shown in Fig. 10(d), then the collecting plate starts to move left. With the continuous leftward movement of the collecting plate, the liquid line between the nozzle and the deposition plate transitions from compression to stretching process, as shown in Figs. 10(e)–10(g). In this process, droplets at the nozzle receive less traction due to their large viscosity, and droplets at the nozzle still gather at the right side of the nozzle center. Figs. 10(h)–10(l) illustrate the process of the nozzle liquid line contacting the top surface of the deposited second layer, from deposition to stable deposition. Fig. 10(h) shows the state of the liquid line when stretched to the limit position, and at this time the liquid line is stretched into a straight overhanging state. With the continuous movement of the collecting plate to the left, the liquid line continues to be stretched and lengthened under the action of electric field force, traction force, etc. However, at this time, the bottom liquid line begins to deposit at the surface of the second deposition line under the action of gravity, as shown in Fig. 10(i). Under the action of traction force, droplets at the nozzle gradually change from gathering at the right end to gathering at the left end, as shown in Figs. 10(j)–10(k), and finally begin to undergo stable deposition, as shown in Fig. 10(l). During the stable deposition of the third layer, the liquid line deflection angle $\alpha = 60.52°$, which is larger than the liquid line deflection angle $\alpha = 41.02$ for the first layer. This is attributed to the fact that the height of the first two layers of printed material deposited when the third layer is written directly is less than 0.2 mm of the height raised by the nozzle, which increases the height between the nozzle and the deposition surface.

Fig. 11 shows a micro "wall" structure with 10 printing layers and 60 mm length. Fig. 11(a) exhibits the overall macro image, and Figs. 11(b) and 11(c) display the front and top views of the "wall" structure, respectively. Figs. 11(d) and 11(e) show the enlarged morphology of the two structures, respectively. These figures show that the line width and height of the structure are in good agreement. The deposition widths of four segments were measured to be 120.15, 122.76, 121.99, and 121.60 μm, respectively. The average line width of the deposited structure is 121.63 μm. Fig. 12 shows the longitudinal cross-section profile of the "wall" structure, and Fig. 12(a) exhibits its 3D morphology. Fig. 12(b) exhibits that the longitudinal cross-section profiles are similar in shape, and the two side profiles are slightly closer to the center, showing a very small taper. This is because the first deposited liquid line is not fully solidified, and it is compressed and deformed under the action of gravity of the post-settling liquid line. The measured profile heights are 228.94, 230.96, 227.58, and 230.36 μm. The average height of the structure is 229.46 μm, and its aspect ratio is 1.89:1.

B. Direct writing of the thin-walled ring structure with a large aspect ratio

Fig. 13 shows the shape of a ring structure with a large aspect ratio. The process parameters are consistent with the wall structure; direct writing speed is F60; the number of printing layers is 20; and the ring radius is 6 mm. Fig. 13(a) shows the macro image of the overall structure of the ring, and Figs. 13(b) and 13(c) exhibit the front view and top view
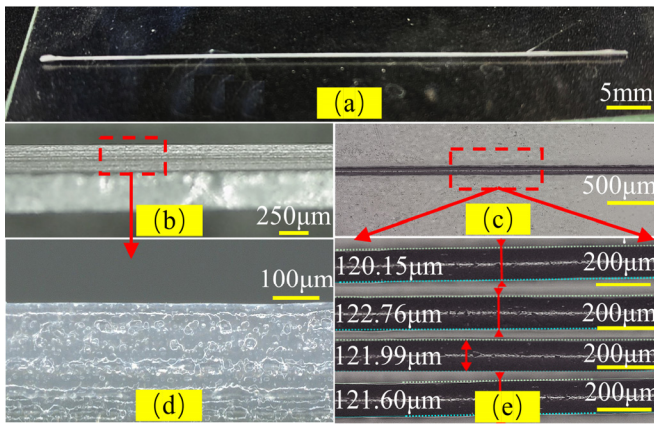
Fig. 11 Structural morphology of micro 'wall' with a large aspect ratio: (a) overall macro image, (b) Front views, (c) Top views, (d) Enlarged view of the front side, and (e) Enlarged view of the top
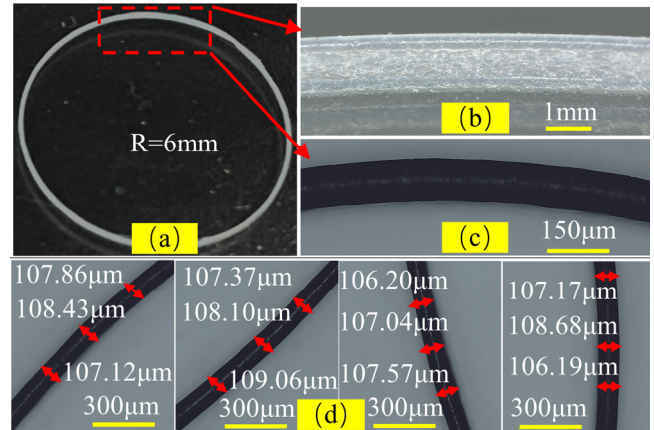

Fig. 13 Structural morphology of large aspect ratio ring: (a) overall macro image, (b) Enlarged view of the front side, (c) Enlarged view of the top, and (d) Ring diameter measurement diagram.
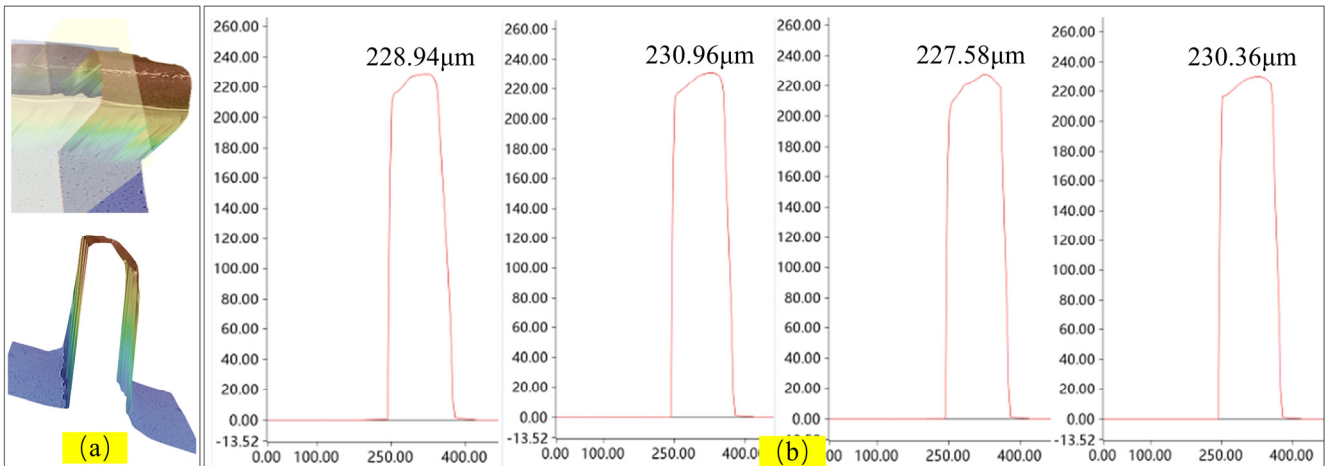

Fig. 12 Longitudinal section outline of micro "wall" structure: (a) The 3D shape of the section. (d) Profile measurement of longitudinal section
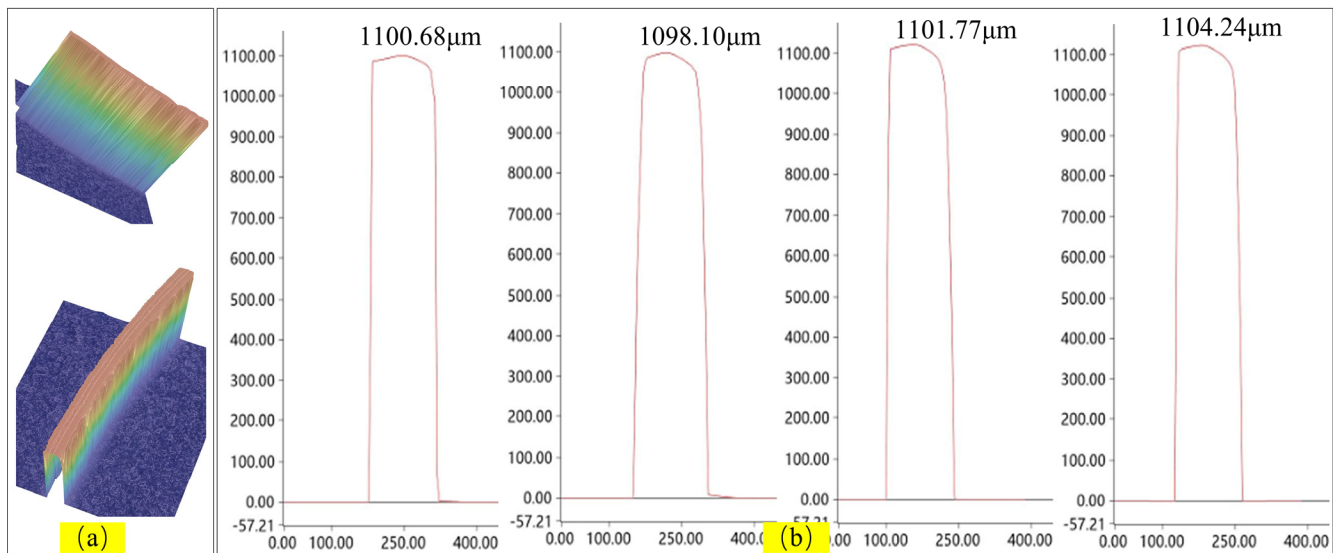

Fig. 14 Large aspect ratio annular longitudinal section outline: (a) The 3D shape of the section, (d) Profile measurement of longitudinal section

of the ring structure, respectively. Four segments were intercepted at four symmetric positions evenly distributed in the circular ring, three measurement points were taken for each segment, as shown in Fig. 13(d), and the average value of its deposition width was measured to be 107.56 μm. Fig. 14 shows the cross-section outline of the ring structure, and its 3D morphology is shown in Fig. 14(a). Fig. 14(b) presents that the shapes of the longitudinal section profiles are similar, and the two side profiles have a very small taper. The measured profile heights are 1100.68, 1098.10, 1101.77, and 1104.24 μm, with an average height of 1101.20 μm. The aspect ratio of the ring is 10.24:1.

VI. CONCLUSION

Biological scaffolds are considered to be one of the most effective therapeutic means in biomedicine, as they eventually degrade *in vivo* after completing their therapeutic mission, thus avoiding the long-term foreign body impact of prosthesis implantation. Micro/nano 3D printing is a new

precision machining technology that offers a new method for processing biological scaffolds. In this study, an electric field-driven melting deposition-based method involving direct writing of high-resolution polycaprolactone (PCL) microstructures was proposed. The effect of collecting plate velocity on the morphology of fiber deposition was studied, and single-layer raster and grid structures, as well as multi-layer "wall" and ring structures, were prepared. The results show that high-performance PCL porous scaffold structures can be fabricated by electric field-driven melting deposition-based direct writing.

REFERENCES

[1] Abhishek Raj, Anand Swarup Chandrakar, Bobby Tyagi, Akash Jain, Hritav Gupta, et al., "Advancements in material extrusion based three-dimensional printing of sensors: a review," International Journal on Interactive Design and Manufacturing (IJIDeM), vol. 18, no.1, pp627–648, 2024.

[2] Velarde-Gomez, Sergio, Alexander Molina-Cabrera, and Eduardo Giraldo, "Model-based Adaptive Control of a 3D Printed Permanent Magnet Synchronous Motor," Engineering Letters, vol. 31, no.4, pp1804-1812, 2023.

[3] Domanski, and Zbigniew, "Damage Statistics in Progressively Compressed Arrays of Nano-pillars," Engineering Letters, vol. 27, no.1, pp18-23, 2019.

[4] Shiyan Yang, Weibo Jiang, Xiao Ma, Zuobin Wang, Robert L Sah, et al., "Nanoscale Morphologies on the Surface of 3D-Printed Titanium Implants for Improved Osseointegration: A Systematic Review of the Literature," International Journal of Nanomedicine, vol. 18, no.1, pp4171-4191, 2023.

[5] Yu Wang, Jiahui Guo, Dongyu Xu, Zhuxiao Gu, and Yuanjin Zhao, "Micro-/nano-structured flexible electronics for biomedical applications," Biomedical Technology, vol. 2, no.1, pp 1-14, 2023.

[6] Han Zhang, Long Huang, Mingyue Tan, Shaoqing Zhao, Hua Liu, et al., "Overview of 3d-printed silica glass," Micromachines, vol. 13, no.1, pp81-102, 2022.

[7] Simon M. Scott and Zulfiqur Ali, "Fabrication methods for microfluidic devices: An overview," Micromachines, vol. 12, no.3, pp319-331, 2021.

[8] Balasubramanian Nagarajan, Zhiheng Hu, Xu Song, Wei Zhai, and Jun Wei, "Development of micro selective laser melting: The state of the art and future perspectives," Engineering, vol. 5, no.4, pp702-720, 2019.

[9] Sheng Bi, Rongyi Wang, Xu Han, Yao Wang, Dongchen Tan, et al., "Recent Progress in Electrohydrodynamic Jet Printing for Printed Electronics: From 0D to 3D Materials," Coatings, vol. 13, no.4, pp1150-1162, 2023.

[10] Hongrui Lin, Haotian Bai, Zhiwen Yang, Qi Shen, Mingyu Li, et al., "Conjugated polymers for biomedical applications," Chemical Communications, vol. 58, no.52, pp7232-7244, 2022.

[11] Zhirui Mai, Qilong Liu, Yongshuang Bian, Peng Wang, Xuewei Fu, et al., "PCL/Collagen/UA Composite Biomedical Dressing with Ordered Microfiberous Structure Fabricated by a 3D Near-Field Electrospinning Process," Polymers, vol. 15, no.1, pp223-242, 2022.

[12] Krishna C. R. Kolan, Jie Li, Sonya Roberts, Julie A. Semon, Jonghyun Park, et al., "Near-field electrospinning of a polymer/bioactive glass composite to fabricate 3D biomimetic structures," International journal of bioprinting, vol. 5, no.1, pp163-182, 2018.

[13] M. García-Galán, F.J. Martínez-Vázquez, N. Rebollo-Munoz, J.M. Montanero, and P. Miranda, "Applicability of near-field electrospinning for the development of TCP-based thin fibres and scaffold 3D printing," Boletín de la Sociedad Española de Cerámica y Vidrio, vol. 62, no.4, pp329-337, 2023.

[14] Zining Wang, Xinliang Ye, Yingxian Lin, Zhishan Tan, Yuming Liu, et al., "Near-Field Direct Write Microfiber-Reinforced Collagen Hydrogel Scaffolds for Articular Cartilage Regeneration," Nano Life, vol. 11, no.4, pp2141002, 2021.

[15] Kai Cao, Fucheng Zhang, Ahmadreza Zaeri, Ralf Zgeib, and Robert C. Chang, "Quantitative investigation into the design and process parametric effects on the fiber-entrapped residual charge for a polymer melt electrohydrodynamic printing process," Macromolecular Materials and Engineering, vol. 307, no.3, pp2100766, 2022.

[16] Gernot Hochleitner, Tomasz Jüngst, Toby D Brown, Kathrin Hahn, Claus Moseke, et al., "Additive manufacturing of scaffolds with sub-micron filaments via melt electrospinning writing," Biofabrication, vol. 7, no.3, pp035002, 2015.

[17] Chiara Großhaus, Ezgi Bakirci, Marius Berthel, Andrei Hrynevich, Juliane C. Kade, et al., "Melt electrospinning of nanofibers from medical-grade poly (ε-Caprolactone) with a modified nozzle," Small, vol. 16, no.44, pp2003471, 2020.

[18] Zhijun Chen, Yanbo Liu, Juan Huang, Ming Hao, Xiaodong Hu, et al., "Influences of process parameters of near-field direct-writing melt electrospinning on performances of polycaprolactone/nano-hydroxyapatite scaffolds," Polymers, vol. 14, no.16, pp3404-3418, 2022.

[19] Zhijun Chen, Yanbo Liu, Juan Huang, Han Wang, Ming Hao, et al., "Enhanced In Vitro Biocompatible Polycaprolactone/Nano-Hydroxyapatite Scaffolds with Near-Field Direct-Writing Melt Electrospinning Technology," Journal of Functional Biomaterials, vol. 13, no.4, pp161, 2022.

[20] Yubo Shi, Lei Wang, Liguo Sun, Zhennan Qiu, Xiaoli Qu, et al., "Melt electrospinning writing PCL scaffolds after alkaline modification with outstanding cytocompatibility and osteoinduction," International Journal of Bioprinting, vol. 9, no.6, pp1071-1089, 2023.

[21] Guangming Zhang, Hongbo Lan, Lei Qian, Jiawei Zhao, and Fei Wang, "A microscale 3D printing based on the electric-field-driven jet," 3D Printing and Additive Manufacturing, vol. 7, no.1, pp37-44, 2020.

[22] Zhi Wang, Guangming Zhang, Hui Huang, Lei Qian, Xiaoling Liu, et al., "The self-induced electric-field-driven jet printing for fabricating ultrafine silver grid transparent electrode," Virtual and Physical Prototyping, vol. 16, no.1, pp113–123,2021.

[23] Livio Gamba, Santiago Diaz-Arauzo, Mark C. Hersam, and Ethan B. Secor, "Aerosol Jet Printing of Phase-Inversion Graphene Inks for High-Aspect-Ratio Printed Electronics and Sensors," ACS Applied Nano Materials, vol. 6, no.22, pp21133-21140, 2023.